

Calibration of the EDELWEISS Cryogenic Heat-and-ionisation Germanium Detectors for Dark Matter Search

The EDELWEISS Collaboration:

O. Martineau¹, A. Benoît², L. Bergé³, A. Broniatowski³, L. Chabert¹,
B. Chambon¹, M. Chapellier⁴, G. Chardin⁵, P. Charvin^{5,6}, M. De Jésus¹, P.
Di Stefano¹, D. Drain¹, L. Dumoulin³, J. Gascon¹, G. Gerbier⁵, E. Gerlic¹,
C. Goldbach⁷, M. Goyot¹, M. Gros⁵, J.P. Hadjout¹, S. Hervé⁵, A. Juillard³,
A. de Lesquen⁵, M. Loidl⁵, J. Mallet⁵, S. Marnieros³, N. Mirabolfathi⁶,
L. Mosca^{5,6}, X.-F. Navick⁵, G. Nollez⁷, P. Pari⁴, C. Riccio^{5,6}, V. Sanglard¹,
L. Schoeffel⁵, M. Stern¹, L. Vagneron¹

¹Institut de Physique Nucléaire de Lyon-UCBL, IN2P3-CNRS, 4 rue Enrico Fermi,
69622 Villeurbanne Cedex, France

²Centre de Recherche sur les Très Basses Températures, SPM-CNRS, BP 166,
38042 Grenoble, France

³Centre de Spectroscopie Nucléaire et de Spectroscopie de Masse, IN2P3-CNRS,
Université Paris XI, bat 108, 91405 Orsay, France

⁴CEA, Centre d'Études Nucléaires de Saclay, DSM/DRECAM, 91191 Gif-sur-
Yvette Cedex, France

⁵CEA, Centre d'Études Nucléaires de Saclay, DSM/DAPNIA, 91191 Gif-sur-Yvette
Cedex, France

⁶Laboratoire Souterrain de Modane, CEA-CNRS, 90 rue Polset, 73500 Modane,
France

⁷Institut d'Astrophysique de Paris, INSU-CNRS, 98 bis Bd Arago, 75014 Paris,
France

Abstract

Several aspects of the analysis of the data obtained with the cryogenic heat-and-ionisation Ge detectors used by the EDELWEISS dark matter search experiment are presented. Their calibration, the determination of their energy threshold, fiducial volume and nuclear recoil acceptance are detailed.

1 Introduction

The dominant ($\sim 90\%$) component of the mass budget of the Universe may consist in Weakly Interacting Massive Particles (WIMPs), which could be the Lightest Supersymmetric Particles (neutralinos in most models)¹. WIMPs would be present at the galactic scale as a halo of mass typically ten times larger than the visible part of the galaxy. The EDELWEISS collaboration has developed heat-and-ionisation Ge detectors [2] to measure recoils induced by elastic scattering of galactic WIMPs on a target nucleus. Constraints on the spin-independent WIMP-nucleon cross-section in the framework of the Minimal SuperSymmetric Model (MSSM) have been derived from the nuclear recoil rate measured with the EDELWEISS detectors [3], [4]. We present in this paper the experimental details of these measurements. In Section 2, we describe briefly the experimental setup and the method of detection of an energy deposit in the target. We then show the calibration procedure for the heat and ionisation signals (Section 3), the trigger threshold determination (Section 4) and the tagging of the nuclear recoils (Section 5). We finally present an original method to determine the fiducial volume of the detectors (Section 6).

2 The EDELWEISS detectors

2.1 Experimental setup

The experimental setup of the EDELWEISS-I experiment is described in [3] and [4]. We simply recall that up to three detectors can be housed in a low background dilution cryostat working at a regulated temperature (27 mK in [3] and 17 mK in [4]). The EDELWEISS detectors are made of a germanium absorber (target for the incident particles) equipped with a thermal sensor and with metallic electrodes for charge collection. The simultaneous measurement of both phonons and charges created by a single interaction is therefore possible.

The main characteristics of the detectors studied in this article are given in Table 1. For all of these detectors, the absorber is a ~ 320 g Ge cylindrical crystal (~ 70 mm diameter and 20 mm thickness). Their edges have been beveled at an angle of 45° (Fig. 1). The electrodes for ionisation measurement are made of 100 nm Al layers sputtered on the surfaces after etching. The top electrode is divided in a central part and a guard ring, electrically decoupled for radial localization of the charge deposition. The bottom elec-

¹See e.g. [1] for a review.

trode is the common reference. For the GGA1 and GGA3 detectors (GSA1 and GSA3), a 60 nm hydrogenated amorphous germanium (silicon) layer was deposited under the electrodes in order to reduce the charge collection problems associated with events where the energy is deposited close to the detector surface. It has indeed been shown that the probability that charge carriers be collected on the same-sign electrode during the diffusion phase which precedes the charge collection (dead layer problem) is reduced for this type of detectors [5, 6].

The thermal sensor consists of a Neutron Transmutation Doped germanium crystal (NTD)², close to the metal-insulator transition. It is glued on a sputtered gold pad near the edge of the bottom Al electrode (Fig. 1). The resistance of the DC-polarized GeAl6 sensor was chosen to be $\sim 3 \text{ M}\Omega$ for GeAl6 ($T_{running} \sim 27 \text{ mK}$), and ranged from $3 \text{ M}\Omega$ to $6 \text{ M}\Omega$ at 17 mK for the other detectors. Reliable electrical contacts and heat links have been achieved by the ultrasonic bonding of gold wires (diameter $25 \mu\text{m}$) on gold pads. The thickness of these pads has been chosen to minimize the production of dislocations in the absorber caused by the bonding. A thermal analysis of the detectors will be published in Ref. [6].

2.2 Detection method

The rise in temperature due to an energy deposit in the absorber gives rise to a variation ΔR of the thermal sensor resistance. When the sensor is polarized by a constant current I , ΔR then induces a voltage fluctuation ΔV across the resistor, which corresponds to the heat signal:

$$\Delta V = \Delta R \times I \quad (1)$$

The ionisation signal is obtained by collection of the electron-hole pairs created by the interaction in the germanium crystal polarized through a bias voltage applied to the electrodes. A low bias voltage³ is required to limit the heating of the cristal due to the drift of the charge carriers, known as the Neganov-Luke effect [7].

The energy E_R deposited by a particle interacting in the detector can be determined by subtracting the Neganov-Luke effect from the heat signal :

$$E_R = \left(1 + \frac{V}{\varepsilon_\gamma}\right) E_H - \frac{V}{\varepsilon_\gamma} E_I \quad (2)$$

²The NTD thermal sensors have been produced by Torre and Mangin for GeAl6 and by Haller-Beeman Associates for the other detectors.

³During the data takings, the bias voltage applied to the top electrode varied from $\pm 3 \text{ V}$ to $\pm 9 \text{ V}$ depending on the detector.

where V is the bias voltage and $\varepsilon_\gamma = 3 V$ the mean electron-hole pair creation potential in germanium for γ -ray interactions (electron recoils). The variables E_H and E_I stand respectively for the heat and ionisation signal amplitudes calibrated for γ -ray interactions following the procedure described in Section 3.1.

We define the quenching variable Q as:

$$Q = \frac{E_I}{E_H} \quad (3)$$

This variable is of particular interest in the case of WIMP search since nuclear and electronic recoils correspond to different ionisation efficiencies. As E_I and E_H are calibrated using γ -rays, $Q = 1$ for electronic interactions by definition. In the case of nuclear recoils (such as those that would be produced by WIMP interactions), this ratio is much lower: $Q \sim 0.3$. The simultaneous measurement of heat and ionisation therefore provides an event-by-event identification of the type of recoils and thus gives an efficient method to reject the dominant γ -ray background. The precise definition of the rejection criteria is discussed in Section 5.

3 Calibration and resolution of heat and ionisation signals

3.1 Calibration of heat and ionisation channels

The ionisation signal E_I is calibrated using a ^{57}Co source that can be inserted in the liquid He bath of the cryostat to a distance of ~ 10 cm from the detectors, with only a ~ 0.5 cm thick copper shielding layer between the source and the detectors. The 122 and 136 keV peaks are clearly visible on the spectra (Fig. 2c), allowing a precise calibration of the ionisation signal. The linearity of the signal amplitude has been verified using the 46.52 keV line from ^{210}Pb (Fig. 2b) in the detector environment and the 8.98 and 10.37 keV lines from the decay of cosmic-ray induced long life isotopes ^{65}Zn and ^{68}Ge in the detector. The calibration factor is observed to be stable within a fraction of percent over periods of months. Because of the parasite capacitance between the centre and guard electrodes, a charge fully collected on an electrode also induces a signal on the other. This cross-talk of a few percents is purely linear and remains constant in time for a given detector. It can thus be easily corrected off-line (Fig. 3). The ionisation signal E_I is defined as the sum of the guard ring and center electrode signal amplitudes

after correction of the cross-talk and calibration of the two channels.

The heat signal amplitude E_H is periodically calibrated using the same ^{57}Co source. In contrast with ionisation, the heat signal appears to be very sensitive to long term drifts of the NTD temperature. It may for example vary by a few percent during several hours after transfers of cryogenic fluids. Between two ^{57}Co calibrations, the heat signal is therefore monitored on a continuous basis using the data from the low-background physics runs themselves by setting the average value of the Q ratio to 1 for electron recoils. The 46.52 keV line from ^{210}Pb and the 8.98 and 10.37 keV lines associated with cosmogenesis activation of ^{65}Zn and ^{68}Ge in the detector (Fig. 2a) are used to check the quality of the calibration of the heat signal.

It should be stressed again at this point that the heat and ionisation signals are calibrated using γ -ray sources, which induce electron recoils. The E_I and E_H values thus correspond to the actual energy deposit for this type of interactions only, and are therefore expressed in keV electron equivalent (keV_{ee}).

3.2 Resolution of heat and ionisation channels

For each detector, the baseline resolutions of the heat and the two ionisation channels are regularly controlled through runs with an automatic random trigger. These runs show that the noises of the three channels are not correlated. The ionisation baseline resolution can therefore be written as :

$$(\sigma_I^0)^2 = (\sigma_{center}^0)^2 + (\sigma_{guard}^0)^2 \quad (4)$$

The ^{57}Co calibrations give a measurement of the resolutions for the ionisation and heat signals at 122 keV. Typical values obtained for the detectors studied here are given in Table 2.

We parametrize the heat and ionisation signals resolutions at a given electron-equivalent energy E as :

$$\sigma_{I,H}(E) = \sqrt{(\sigma_{I,H}^0)^2 + (a_{I,H}E)^2} \quad (5)$$

where the factors a_I and a_H are deduced from the resolution of the ionisation and heat signals at 122 keV. The resolutions of the 10.37 and 46.52 keV peaks observed in low-background physics runs fit well with the expressions $\sigma_{I,H}(E)$ from Eq. (5) (Fig. 2d). It can be noted that the resolutions at $E_I \sim 10 \text{ keV}_{ee}$ -an energy below which most of the WIMPs signal is expected- is dominated by the baseline resolutions σ_I^0 and σ_H^0 .

Finally, the recoil energy resolution can be computed from the heat and

ionisation signal resolutions using Eq. (2). The noises of both signals being uncorrelated, this resolution can be written as:

$$\sigma_{E_R} = \sqrt{\left(1 + \frac{V}{\varepsilon_\gamma}\right)^2 (\sigma_{E_H})^2 + \left(\frac{V}{\varepsilon_\gamma}\right)^2 (\sigma_{E_I})^2} \quad (6)$$

In the case of GeAl6, and for the bias voltage applied during the low-background physics run ($V=6$ V), the resolution values displayed in Table 2 lead to $\sigma_{E_R} \sim 8$ keV FWHM around 30 keV. This value is reduced to 4 keV FWHM in the condition of the low-background physics run recorded with GGA1 ($V=4$ V) [4].

4 Threshold

The ionisation and heat channel data are continuously digitized and filtered at a rate of 200 kHz and 2kHz, respectively. When a filtered ionisation value exceeds a fixed threshold value, data samples in all detectors are stored to disk. The trigger is defined by requiring a minimum threshold on the absolute value of any of the filtered ionisation channels. For each event, the list of all detectors having triggered is stored as a bit pattern.

The ionisation threshold value, $E_{I,th}$ is defined as the ionisation energy (in keV_{ee}) at which the trigger efficiency reaches 50%. It is the most important parameter governing the recoil energy dependence of the efficiency. Its value is measured using two different techniques: one is based on the Compton plateau observed with a γ -ray source, and the other on coincidence neutron data.

In the first one, a γ -ray spectra is recorded using a source producing a important Compton plateau, such as ^{60}Co or ^{137}Cs . Monte Carlo simulations indicate that the shape of the plateau above 10 keV can be linearly extrapolated to lower energy. The efficiency as a function of E_I , $\epsilon(E_I)$, is thus obtained by dividing the measured rate by the straight line extrapolated from the rate above 10 keV. The resulting $\epsilon(E_I)$ data is fitted by a integral of a gaussian (erf), yielding the experimental value of $E_{I,th}$. However, this method is limited by the large data sample necessary to obtain a significant number of events in the threshold region.

The second technique was made possible by the simultaneous operation of three detectors with a ^{252}Cf neutron source (and thus could not be applied to the GeAl6 detector). Neutron scattering induces a large number of coincidence events where at least two detectors are hit. The upper panel of Fig. 4 shows the E_I distribution recorded in one detector with the condition

that any of the other two detector triggered (unfilled histogram). Despite that the detector under study is not requested in the trigger pattern, the peak at $E_I=0$ due to baseline noise is not overwhelmingly large, due to the importance of the coincident rate. An unbiased sample of events with $E_I > 2$ keV is thus obtained. When in this sample it is further requested that the detector under study be present in the trigger pattern, the shaded histogram is obtained. The ratio of the two distributions shown in the lower pannel of Fig. 4 correspond to the efficiency $\epsilon(E_I)$. This interpretation is valid in the region close to $E_{I,th}$ and above because in that energy range the contribution of the peak due to baseline events is negligible and because the slope of the unbiased distribution is reasonably small compared to the experimental resolution on E_I . Indeed, applying this method to a distribution $N(E_I)$ proportionnal to $\exp(-E_I/\tau)$ and smeared with an experimental r.m.s. resolution σ , this method would result in a shift of $-\sigma^2/\tau$ of the deduced value of $E_{I,th}$ relative to the true value. In the present case, where the range of exponential slopes and resolution are $3 < \tau < 8$ keV and $1 < 2.35\sigma < 2$ keV, the shift should not exceed 0.2 keV.

Both Compton and neutron coincidence techniques give consistent ionisation threshold measurements. The coincidence measurements are the most precise, as the neutron source has the advantage of yielding a maximum rate at the lowest energy, and in addition, the quenching of ionisation for nuclear recoils ensure that the stability of the measurement can be tested by imposing a cut on the heat signal E_H without affecting the ionisation signals with E_I above $\sim E_H/2$. The measured $E_{I,th}$ values for the different ionisation channels of the detectors under study are listed in the last column of Table 2.

5 Nuclear recoil band

Figure 5 shows a (E_R, Q) distribution from the data recorded with a ^{252}Cf source emitting γ -rays and neutrons. Experimentally, the Q variable appears to follow a gaussian distribution at the $\sim 2\sigma$ level for both nuclear and electron recoils populations (Fig. 6). We therefore parametrize the region of 90% acceptance for the nuclear recoils by the following cut:

$$|Q - \langle Q_n \rangle| \leq 1.65\sigma_{Q_n} \quad (7)$$

where $\langle Q_n \rangle$ and σ_{Q_n} are the average value and the standard deviation of the Q distribution for nuclear recoils, both variables being determined for each detector from ^{252}Cf calibration data under the same experimental conditions as the low-background physics runs.

5.1 Neutron line

The neutron line is the average Q value for the nuclear recoils population. It is parametrized from ^{252}Cf calibration data by :

$$\langle Q_n \rangle (E_R) = a (E_R)^b \quad (8)$$

The a and b values resulting from the fit of the experimental data for each EDELWEISS detector are statistically consistent with the values $a = 0.16$ and $b = 0.18$ quoted in [8]. The biases on the determination of $\langle Q_n \rangle$ due to experimental calibration uncertainties, heat quenching effects [9], and multiple scatterings are globally taken into account with this measurement.

5.2 Electron and nuclear recoils zones standard deviations

The standard deviation of the electronic and nuclear recoil distributions, respectively noted σ_{Q_γ} and σ_{Q_n} , can be calculated with Eqs. (2) and (3) by propagation of the experimental values σ_I and σ_H :

$$\begin{aligned} \sigma_{Q_\gamma}(E_R) &= \frac{(1 + V/3)}{E_R} \sqrt{\sigma_I^2 + \sigma_H^2} \quad (9) \\ \sigma_{Q_n}^0(E_R) &= \frac{1}{E_R} \sqrt{\left(1 + \frac{V}{3} \langle Q_n \rangle\right)^2 \sigma_I^2 + \left(1 + \frac{V}{3}\right)^2 \langle Q_n \rangle^2 \sigma_H^2} \quad (10) \end{aligned}$$

In the case of ^{60}Co , ^{252}Cf calibrations and low-background physics runs, the experimental values of σ_{Q_γ} at high energy are significantly larger (up to $\sim +30\%$ at 122 keV) than those calculated from the resolutions given in Table 2 with Eqs. (4), (5) and (9) (Fig. 7a). A dependance of the heat signal amplitude on the position of the interaction provides an explanation for this discrepancy. This hypothesis is consistent with the $\sim 1\%$ heat signal amplitude difference observed between center and guard events in ^{57}Co calibrations. We therefore enlarge the a_H coefficient in Eq. (5) so that the analytic expression given in Eq. (9) for $\sigma_{Q_\gamma}(E_R)$ actually follows the experimental distribution for ^{60}Co , ^{252}Cf and low-background physics runs. We have checked that 90% of the experimental events then fall inside the electron recoil zone defined in this way.

Even after correcting the a_H value, the nuclear recoils Q distribution of ^{252}Cf calibration data is broader at high energy than what is expected from Eq. (10) (Fig. 7b). Atomic scattering processes [11], fluctuations in the number of charges created by a nuclear recoil [12] and multiple scattering (see Section

5.3) are in particular expected to give an intrinsic width to the Q distribution for nuclear recoils and thus explain this behavior. The experimental σ_{Q_n} dependance on recoil energy is properly described when a constant C is quadratically added to the term associated with the experimental resolution. The equation (10) is thus re-written as follows:

$$\sigma_{Q_n}(E_R) = \sqrt{\sigma_{Q_n}^0(E_R) + C^2} \quad (11)$$

Typical values of $C \sim 0.040$ are determined for each EDELWEISS detector by fitting the experimental σ_{Q_n} points using Eq. (11). With this definition, we have checked for each detector that 90% of nuclear recoils induced by ^{252}Cf calibrations are inside the nuclear recoil zone defined in Eq. (7).

5.3 Effect of multiple scattering

The nuclear recoil zone is determined through neutron calibrations, for which the proportion of multiple interactions is around 40% between 20 and 200 keV. This is of particular importance because in contrast to neutrons, WIMPs are expected to interact only once in the detector, and the Q variable is in this case larger than when the same energy is deposited in multiple nuclear interactions, as can be deduced from Eq. (8).

We therefore evaluated quantitatively the effect of multiple interactions using a GEANT [10] simulation of ^{252}Cf calibrations of the EDELWEISS detectors. The Q variable has been calculated for the simulated nuclear events by associating with Eq. (8) an ionisation signal of amplitude $e_I = 0.16 (e_R)^{1.18}$ to an energy deposit e_R in a single interaction, and summing each individual e_I to obtain the total E_I energy for a given neutron. The effect of multiple interactions has then been evaluated with these simulated data by smearing the resulting Q distribution with the experimental resolution given in Eq. (10), and then by comparing the distributions obtained when selecting or not single interactions events (Fig. 8).

Although multiple interactions tend to lower $\langle Q_n \rangle$, this effect remains weak, and the Q distribution associated with single interactions events is only slightly narrower and completely included in the wider band. The nuclear recoils zone determined through ^{252}Cf calibrations has therefore been conservatively used for the low-background physics run analysis.

5.4 Analysis energy range

Equations (9) and (10) predict that the discrimination between electronic and nuclear interactions is deteriorated at low energies (see also Fig. 5).

Rejection of the γ -ray background at a given level therefore defines a lower bound for the analysis energy range.

Secondly, the detection efficiency has to be as close to 100% as possible in the analysis window in order to insure a good quality for the data set. The trigger threshold is therefore another factor which has to be taken into account for the definition of the analysis lower energy bound. For both 2000 [3] and 2002 [4] runs, the choice of the analysis lower bound has mainly been driven by this last factor. The threshold values of 5.7 and 3.5 keV_{ee} for the ionisation signal indeed correspond respectively to recoil energies of 30 and 20 keV for a 100% detection efficiency, and 90% efficiency when the nuclear recoil zone is taken into account.

Extensive γ -rays and neutron calibrations are performed before the physics data taking is initiated in order to fix the lowest recoil energy value corresponding to acceptable levels of γ -ray background rejection and detection efficiency. This ensures that the lower limit of the analysis window is not influenced by the possible presence of events in the final data set. The definition of the upper bound of the analysis window is described in [4].

6 Fiducial volume

6.1 Modelisation of the collection process

The segmentation of the upper charge collection electrode in a central part and a guard ring leads to the definition of a fiducial volume. This volume is shielded against a significant amount of the radioactivity of the detector environment by the peripheral volume, as shown in [3]. To allow for the experimental resolution on the ionisation signals, the fiducial cut is defined as corresponding to a fraction of 3/4 of the charge collected on the center electrode. In order to give a robust and precise estimation of the detector volume associated with this fiducial cut, it is necessary to relate a given ratio of the two ionisation signal amplitudes to a given volume inside the detector. This is not a straightforward process: first, for non-WIMP interactions, multiple interactions have to be taken into account, and furthermore, interactions between charges may play a crucial role in the collection process. In particular, the important proportion of events with a charge signal shared between the two channels observed in each detector for ^{60}Co calibrations (see e.g. Fig. 3) hints to the importance of these charge interactions processes. In order to test their influence on the determination of the fiducial volume, we choose to model the collection process with the simplified phenomenological description of charge collection given in Ref. [13], associated with the

hypothesis of a plasma effect before charge drift. We will see that, even if some of our results cannot be explained in the framework of this very simplified model (Section 6.2), it provides a good empirical tool to determine the fiducial volume and estimate systematic errors on its value (Section 6.3). The model used here assumes the distribution of the charges in a sphere with uniform density, extending to a maximal radius r_b before the charge is fully collected. Charges are distributed among the two electrodes depending on the position of the interaction relative to the surface corresponding to the separation between drift lines going to the center and guard rings. Here, we assume for simplicity that this surface is parametrized by a cylinder of radius R_C (Fig. 11). For an interaction at the radius $R > R_C + r_b$ in the crystal, the whole charge is fully associated with the guard ring. If $R < R_C - r_b$, then the charge has to be associated with the center electrode. Finally, if $R_C + r_b > R > R_C - r_b$, then the charge is splitted among the two electrodes, with a relative proportion associated with the center electrode corresponding to the fraction of the sphere inside the cylinder of radius R_C . For given values of r_b and R_C , the fiducial volume is determined in this model by the following expression of the fiducial radius:

$$R_{fid} = R_C + 2 \cos\left(\frac{13\pi}{9}\right) r_b \quad (12)$$

A fraction of 1/4 of the total volume of a sphere of radius r_b centered on R_{fid} is inside the cylinder of radius R_C . In the framework of our model, interactions inside the cylinder of radius R_{fid} thus correspond to a charge collection equal or greater than 3/4 of the total charge.

6.2 Validity and limits of the modelisation

In order to test its ability to reproduce the distribution of charge amplitudes, ionisation signals are simulated in the framework of this simple model, using the program GEANT [10] for ^{60}Co and ^{252}Cf calibrations, as described in Section 5.3. The parameters r_b and R_C of the simulated data are then adjusted to match the experimental distribution of the Y variable on a given energy range, the Y variable being defined as the normalized difference of the ionisation signals:

$$Y = \frac{E_{guard} - E_{center}}{E_{guard} + E_{center}} \quad (13)$$

The result of this optimisation is shown in Fig. 9 in the case of a ^{60}Co calibration of the GeAl6 detector under 6.3 V bias voltage. The shape of the simulated distribution closely follows that of the experimental data, while

a simulation using an alternative model (linear distribution of the charge, detailed in [14]) clearly exhibits a different pattern.

We have also studied the evolution of the (r_b, R_C) parameters as a function of bias voltage for the GeAl6 detector [15]. R_C should not depend on the value and sign of the bias voltage, since it is related to the static field distribution only, while r_b should increase with decreasing bias voltage: as the field increases, the less time there is for diffusion processes. The values of the parameters r_b and R_C determined for ^{60}Co and ^{252}Cf calibrations of the GeAl6 detector versus the applied field are displayed in Fig. 10. The r_b and R_C values follow the expected behavior. Moreover, the mean measured value of R_C ($\langle R_C \rangle = 24.45 \pm 0.05$ mm) is statistically compatible with the value $R_{electro} = 24.4$ mm expected from numerical calculations of the electric potential inside this detector (see Table 1).

The very large r_b values are a clear sign that macroscopic charge extension perpendicular to the drift direction occurs before the charge collection is completed. However the data does not support that this expansion is driven by the plasma effect invoqued in Ref. [13]: a charge cloud size of the order or above a millimeter is indeed not compatible with results of studies on the dead layer [5, 16]. Furthermore, Fig. 10 shows that $r_b(-) \ll r_b(+)$ and that the values of r_b for ^{60}Co and ^{252}Cf calibrations do not differ significantly for a same bias voltage. These two experimental results are also in strong disagreement with the predictions derived from the hypothesis of a plasma effect: firstly, the observed asymmetry for r_b values between positive and negative bias voltage does not find any explanation in the framework of the plasma model, and secondly, the plasma effect should be weaker in the case of ^{60}Co calibrations than for ^{252}Cf (and thus r_b values much smaller), since γ -rays induce much lower charge densities than neutrons. These are strong indications that the simple model presented here does not provide a proper description of the dynamics of the charge drift and collection. Charge repulsion during drift, not taken into account here, could for example play an important role in the collection process. A more detailed study, with dedicated detectors, has been initiated in the EDELWEISS collaboration in the aim of better understanding the collection process [16].

6.3 Measurement of the fiducial volume

Our results clearly point out the limits of the modelisation presented in Section 6.1. Still, it has to be stressed that this model reproduces correctly the distribution of charges among the electrodes (Fig. 9), which represents the net effect of the charge collection process. It is therefore sufficient to give a

precise determination of the fiducial volume and evaluate possible systematic errors, before a better, physically motivated model replaces it.

We have calculated R_{fid} with Eq. (12) and the r_b and R_C values determined from ^{252}Cf calibrations under the same bias voltage as that of the low-background physics run for each detector. For all detectors except GeAl10, the R_C values are compatible with those expected from the geometry of the electrodes and from numerical simulations of the electric potential inside the detectors. The values determined for R_{fid} for the detectors are summarized in Table 3. The systematic error associated with the uncertainty on the exact mechanism producing the charge expansion is evaluated by taking the difference between the fiducial volume value deduced using the linear model and the one presented in Section 6.1. Despite the poor description of the charge distribution by the linear model (see Fig. 9), this difference is only 1%. The variation of the energy range used to determine the values of r_b and R_C through comparison of the experimental and simulated Y distributions proved to be a minor contribution to this systematic error.

An alternative evaluation of the fiducial volume is the fraction of cosmic activation events at 8.98 and 10.37 keV (see Fig. 2) selected by the fiducial volume cut. Such events are expected to be evenly spread inside the detector, and are observed at rates varying between 3 to 15 events per detector per day. In the few days following a neutron calibration, the 10.37 keV rate is also enhanced due to ^{71}Ge activation ($T_{1/2} = 2.7$ d), a population that is also expected to be evenly spread inside the detector. The measured fractions, directly interpreted as V_{fid} values, are listed in the last column of Table 3. They are compatible within statistics with the values derived from the neutron calibration data and the collection process modelisation. The cosmic activation data is however less precise due to statistics, but this measurement is a good cross-check for the determination of the fiducial volume, and validates the use of the model presented in Section 6.1 to determine the fiducial volume.

7 Conclusion

We have described in the present work the calibration aspects of the data analysis in the EDELWEISS experiment. In particular, the nuclear recoil zone and fiducial volume have been estimated using several methods, allowing to define a conservative value of these important parameters. A simple parametrization allows us to reproduce accurately the distribution of the charges between the centre and guard electrodes associated with ^{60}Co and

^{252}Cf calibrations, making possible the systematic studies necessary to establish the robustness of the determination of the fiducial volume of the detectors.

References

- [1] L. Bergström, Rep. Prog. Phys **63**, 793 (2000).
- [2] X.F. Navick *et al.*, NIM A **444**, 361 (2000).
- [3] A. Benoît *et al.*, Phys. Lett. B **479** 8 (2000).
- [4] A. Benoît *et al.*, Phys. Lett. B **545** 43 (2002).
- [5] P. Luke *et al.*, IEEE Trans. Nucl. Sci. 41 (4) (1994) 1074.
T. Shutt *et al.*, NIM A **444**, 340 (2000).
T. Shutt *et al.*, in Proc. *9th Int. Workshop on Low Temperature Detectors*, AIP conference proceedings **605**, 513 (2001).
- [6] XF. Navick *et al.*, to be published.
- [7] B. Neganov and V. Trofimov, USSR patent No 1037771, Otkrytia i izobreteniya **146**, 215 (1985).
P.N. Luke, J. Appl. Phys. **64**, 6858 (1988).
- [8] P. Di Stefano *et al.*, Astropart. Phys. **14**, 329 (2001).
- [9] E. Simon *et al.*, NIM A **507**, 643 (2003).
- [10] R. Brun *et al.*, *GEANT3*, CERN report DD/EE/84-1 (1987).
- [11] J. Lindhard *et al.*, Mat. Phys. Medd. Dan. Vid. Selsk **10**, 1 (1963).
- [12] T. Yamaya *et al.*, NIM **159**, 181 (1979).
- [13] M.J. Penn *et al.*, in Proc. *6th Int. Workshop on Low Temperature Detectors*, NIM A **370**, 215 (1996).
- [14] O. Martineau *et al.*, in Proc. *9th Int. Workshop on Low Temperature Detectors*, AIP conference proceedings **605**, 505 (2001).
- [15] O. Martineau, Recherche de WIMPs par l'expérience EDELWEISS: caractérisation des détecteurs et analyse des données, PhD thesis, Université Lyon I (2002) (in french).
Available at <http://edelweiss.in2p3.fr/pub/fichiers/theses.html>.

- [16] A. Broniatowski *et al.*, in Proc. *9th Int. Workshop on Low Temperature Detectors*, AIP conference proceedings **605**, 521 (2001).
A. Broniatowski, to be published in LTD10 proceedings (Genova, July 2003).

Label	Mass (g)	$R_{electro}$ (mm)	Vol. NTD (mm ³)	Amorphous layer	$T_{running}$ (mK)
GeAl6	321.62	24.4	4.0	none	27
GeAl9	325.43	24.0	5.6	none	17
GeAl10	323.91	24.0	5.6	none	17
GGA1	318.50	24.0	1.64	Ge	17
GGA3	324.40	24.0	5.6	Ge	17
GSA1	313.68	24.0	5.6	Si	17
GSA3	297.03	24.0	5.6	Si	17

Table 1: *Main parameters for the EDELWEISS detectors studied in this article. " $R_{electro}$ " refers to the radius value of the cylindrical volume associated with charge collection on the center electrode. These values are calculated through electrostatic simulation of the detector, taking into account the actual electrodes geometry. The existence of an amorphous Ge or Si layer under the electrodes is also mentioned. " $T_{running}$ " is the value of the regulated cryostat temperature while running.*

Detector	FWHM @ 0 keV			FWHM @ 122 keV		Trigger Threshold	
	Center (keV _{ee})	Guard (keV _{ee})	Heat (keV _{ee})	Ion. (keV _{ee})	Heat (keV _{ee})	Center (keV _{ee})	Guard (keV _{ee})
GeAl6	2.0	1.4	2.2	2.8	3.5	6.0	4.0
GeAl9	1.2	1.4	0.5	2.6	3.3	4.3	4.9
GeAl10	1.1	1.3	0.4	3.0	3.5	3.3	4.3
GGA1	1.3	1.3	1.3	2.8	3.5	3.5	3.5
GGA3	1.3	1.5	0.4	3.1	2.7	2.9	3.9
GSA1	1.2	1.4	0.6	3.1	2.8	3.5	3.4
GSA3	1.1	1.3	1.4	3.3	3.3	3.0	3.4

Table 2: Typical values obtained in keV_{ee} for the full width half maximum resolution for heat and ionisation signals at 0 and 122 keV for the detectors studied in this article. The precision on these measurements are ± 0.1 keV at 0 keV and $\sim \pm 0.2$ keV at 122 keV. Also given here are the threshold values for the center and guard channels. The precision is ± 0.1 keV for both channels, except for GeAl6 where it is ± 0.5 keV.

Detector	Bias (V)	r_b (mm)	R_C (mm)	R_{fid} (mm)	V_{fid} (%)	Activation V_{fid} (%)
GeAl6	+6.34	4.3 ± 0.2	24.5 ± 0.3	23.0 ± 0.3	54.6 ± 1.4	50 ± 3
GeAl9	+2.00	6.1 ± 0.2	23.5 ± 0.4	21.4 ± 0.4	47.4 ± 2.0	53 ± 4
GeAl10	-3.00	2.3 ± 0.2	21.9 ± 0.4	21.1 ± 0.4	46.0 ± 1.7	50 ± 4
GGA1	-4.00	1.6 ± 0.1	24.6 ± 0.2	24.1 ± 0.2	60.1 ± 1.1	57 ± 3
GGA3	-4.00	1.4 ± 0.1	24.1 ± 0.2	23.6 ± 0.2	57.7 ± 0.7	60 ± 5
GSA1	-4.00	1.5 ± 0.1	24.2 ± 0.2	23.7 ± 0.2	58.3 ± 0.8	61 ± 4
GSA3	-4.00	1.5 ± 0.1	23.9 ± 0.2	23.3 ± 0.2	56.2 ± 0.8	61 ± 5

Table 3: Values of various parameters for the EDELWEISS bolometers determined from ^{252}Cf calibrations under the given bias voltage. The error bars correspond to statistical errors. The systematic error on V_{fid} is $\sim 1\%$. "Activation" refers to the fraction of 8.98 and 10.34 keV events recorded with the fiducial volume cuts ($E_{center} > 3E_{guard}$).

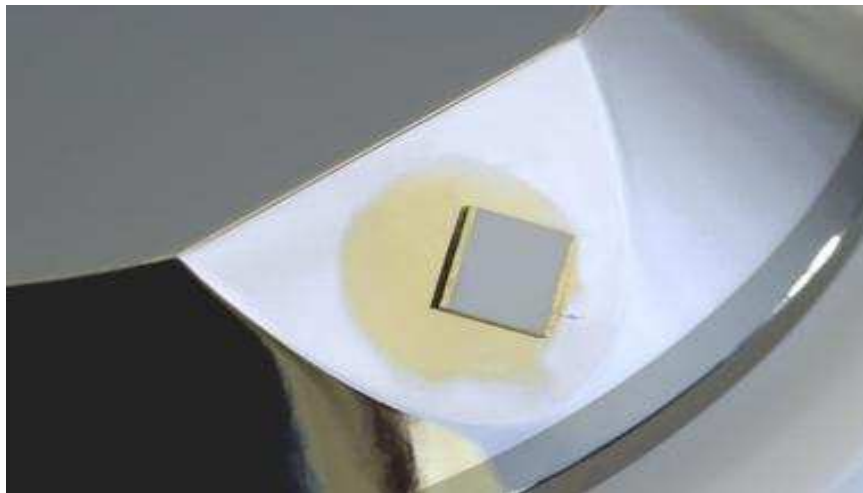


Figure 1: *Top pannel: EDELWEISS GGA1 detector ($\Phi = 70$ mm). Bottom pannel: close-up on the NTD thermal sensor glued on its golden pad on the beveled part of the crystal.*

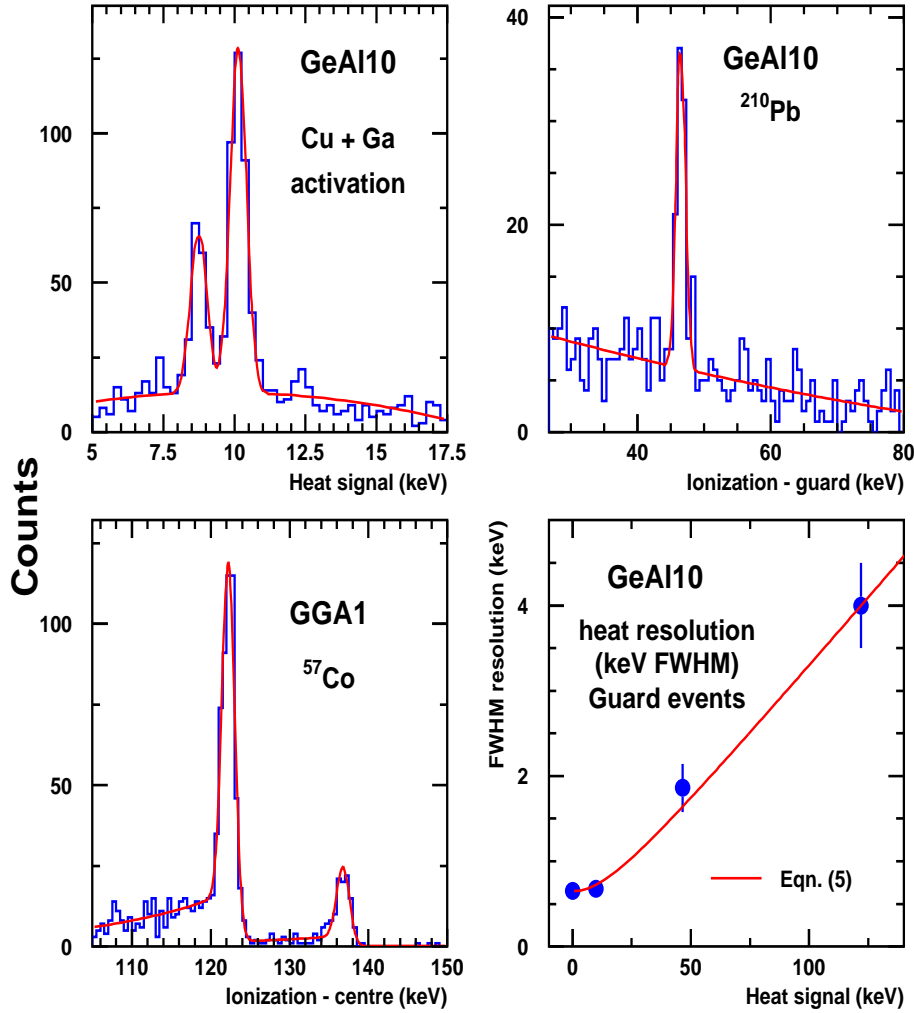


Figure 2: Figs. a), b), c): spectra obtained with the GeAl10 and GGA1 detectors in various energy regions during physics background runs (a and b) and ^{57}Co calibration runs (c). For the first two spectra, the lines associated with ^{65}Zn (8.98 keV) and ^{68}Ge decays (10.37 keV) (a) and ^{210}Pb contamination (46.52 keV) (b) are clearly visible. In Fig. d), the baseline and peak resolutions of the GeAl10 detector heat channel for the 10.37, 46.52 and 122.1 lines are fitted by the expression given in Eq. (5).

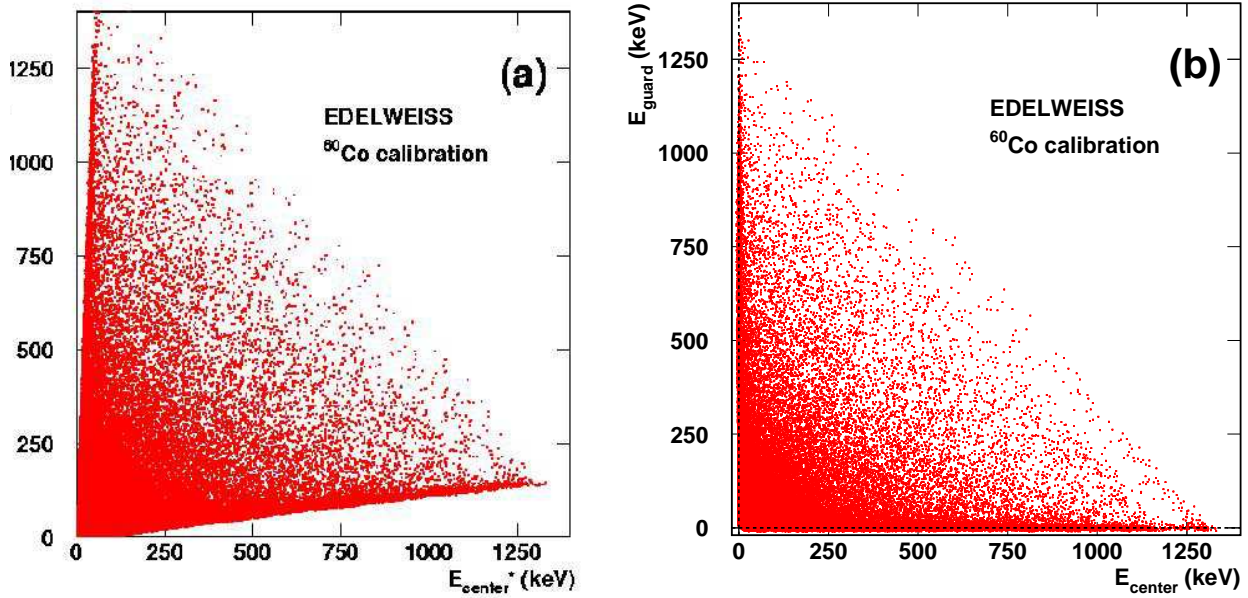


Figure 3: *Distribution of the guard ring versus the center electrode signals for a ^{60}Co calibration of the GeAl6 detector at a bias voltage of +6.34 V before (a) and after (b) linear correction of the cross-talk between the two channels. On Fig. (b), the events along the horizontal (vertical) axis correspond to center (guard) events, for which the charge is fully collected on the center electrode (guard ring), and the events between the two axis correspond to shared events. Shared events represent a proportion of $\sim 50\%$ of the total number of events for this calibration.*

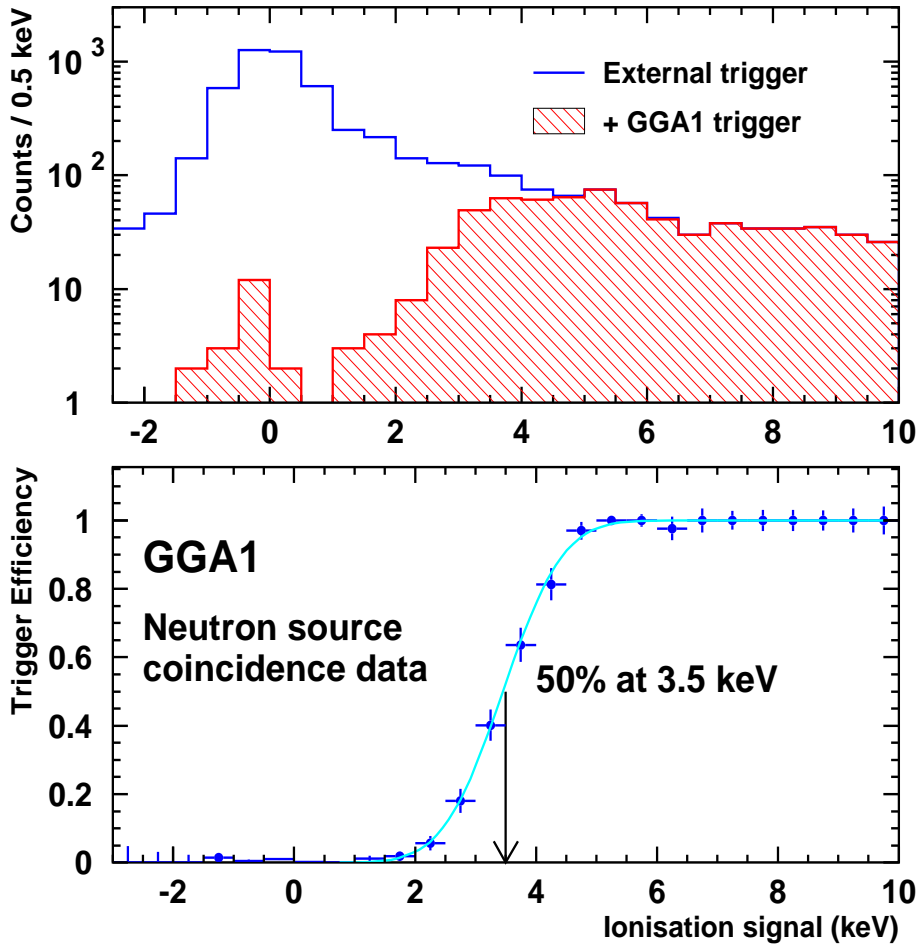


Figure 4: *Top pannel: plot of the data recorded in the GGA1 detector during neutron calibration for any other detector (GeAl9 or GeAl10) triggering (line), and with the additional condition that GGA1 also triggers (hatched area). Bottom pannel: experimental efficiency curve for the GGA1 detector corresponding to the ratio of the two distributions from the top pannel. The 100% efficiency is reached at 5.5 keV_{ee} energy, corresponding to 20 keV recoil energy.*

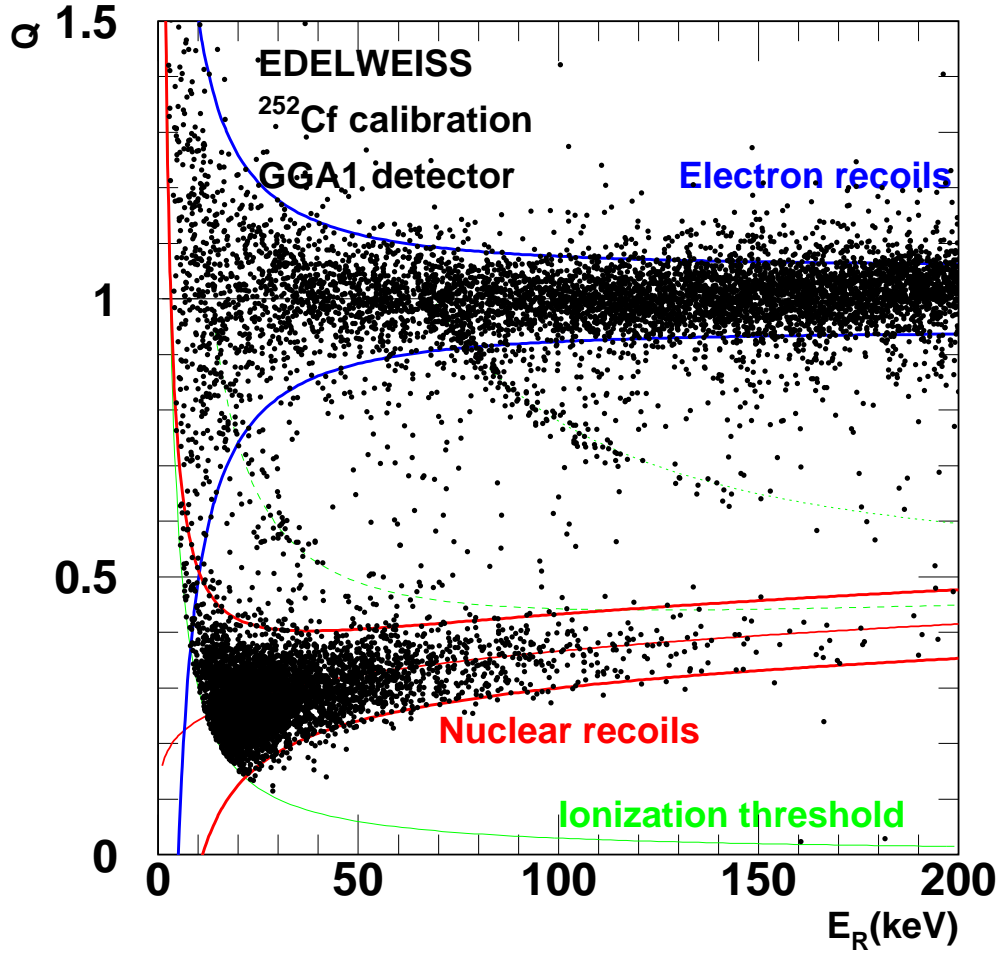


Figure 5: Projection in the (E_R, Q) plane of the events recorded in the GGA1 detector during a ^{252}Cf calibration. The thick lines represent the 90% nuclear and electronic recoils zone ($\pm 1.645\sigma$ around $\langle Q_n \rangle$ and $\langle Q_\gamma \rangle$ respectively). The dotted line corresponds to the ionisation threshold curve ($E_I = 3.5 \text{ keV}_{ee}$ in this case). The dashed lines show where events associated with the inelastic scattering of neutrons on ^{73}Ge (13.26 and 68.75 keV excited levels) are expected in this plane.

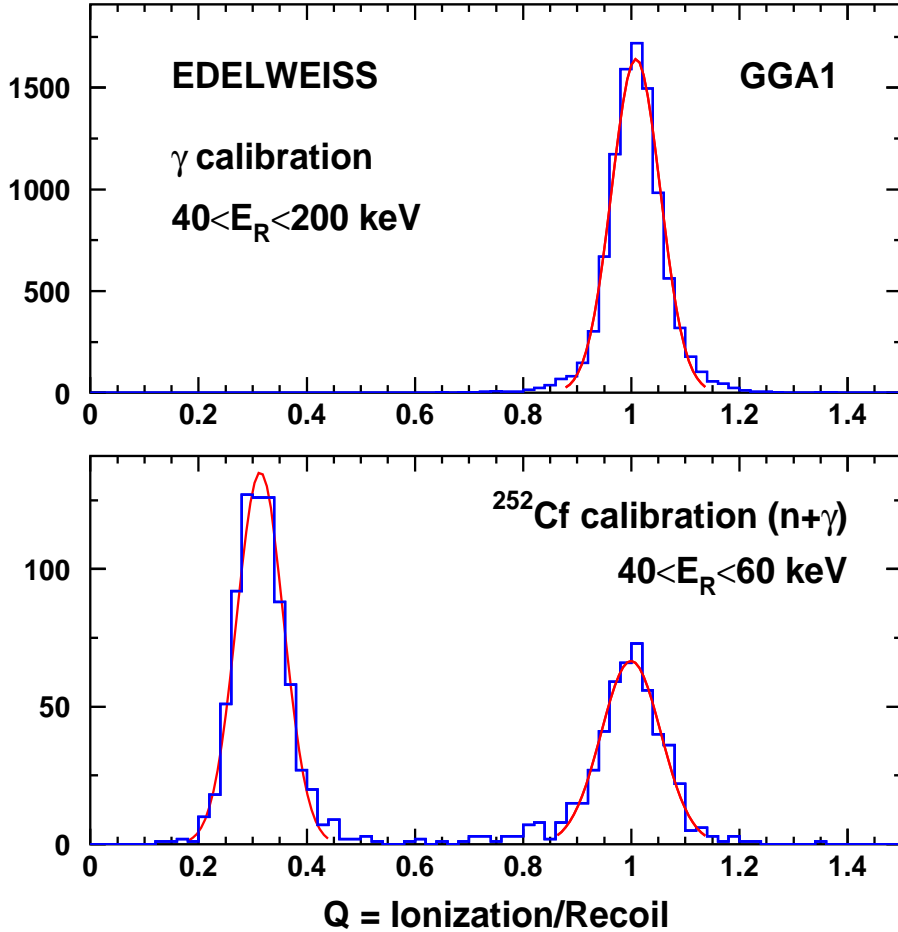


Figure 6: *Top pannel: spectrum of the Q variable in the 40-200 keV recoil energy range for events recorded in the GGA1 detector during a ^{60}Co calibration (electron recoils). No events are seen for $Q < 0.6$. This shows the excellent quality of the charge collection for this detector. This test is performed for every detector before a low-background physics run is started. Bottom pannel: Spectrum of the Q variable in the 40-60 keV recoil energy range for events recorded in the GGA1 detector during a ^{252}Cf calibration (nuclear and electronic recoils). As the fit shows, the nuclear and electron recoils populations follow gaussian distributions down to the 2σ level.*

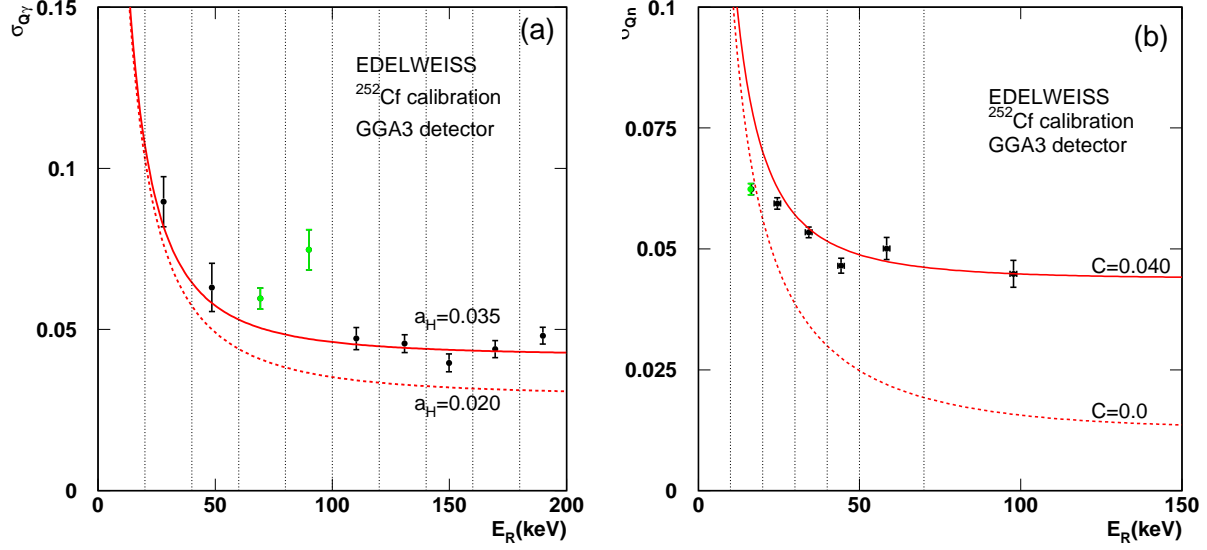


Figure 7: *Experimental values for σ_{Q_γ} (a) and σ_{Q_n} (b) for a ^{252}Cf calibration of the GGA3 detector. Also shown are the computed laws for these two variables from Eqs. (9) and (11), before (dotted line) and after (solid line) correction of the a_H factor for (a), and for $C=0$ (dotted) and $C=0.040$ (solid) for (b). The large value of σ_{Q_γ} in (a) in the 60-80 and 80-100 keV recoil energy bins (bright color) is due to the inelastic scattering events (Fig. 5), while the low value of σ_{Q_n} in (b) in the 10-20 keV energy range (bright color) is related to the ionisation threshold, which artificially narrows the nuclear recoils distribution for low energies. The vertical dashed lines correspond to the bins limits.*

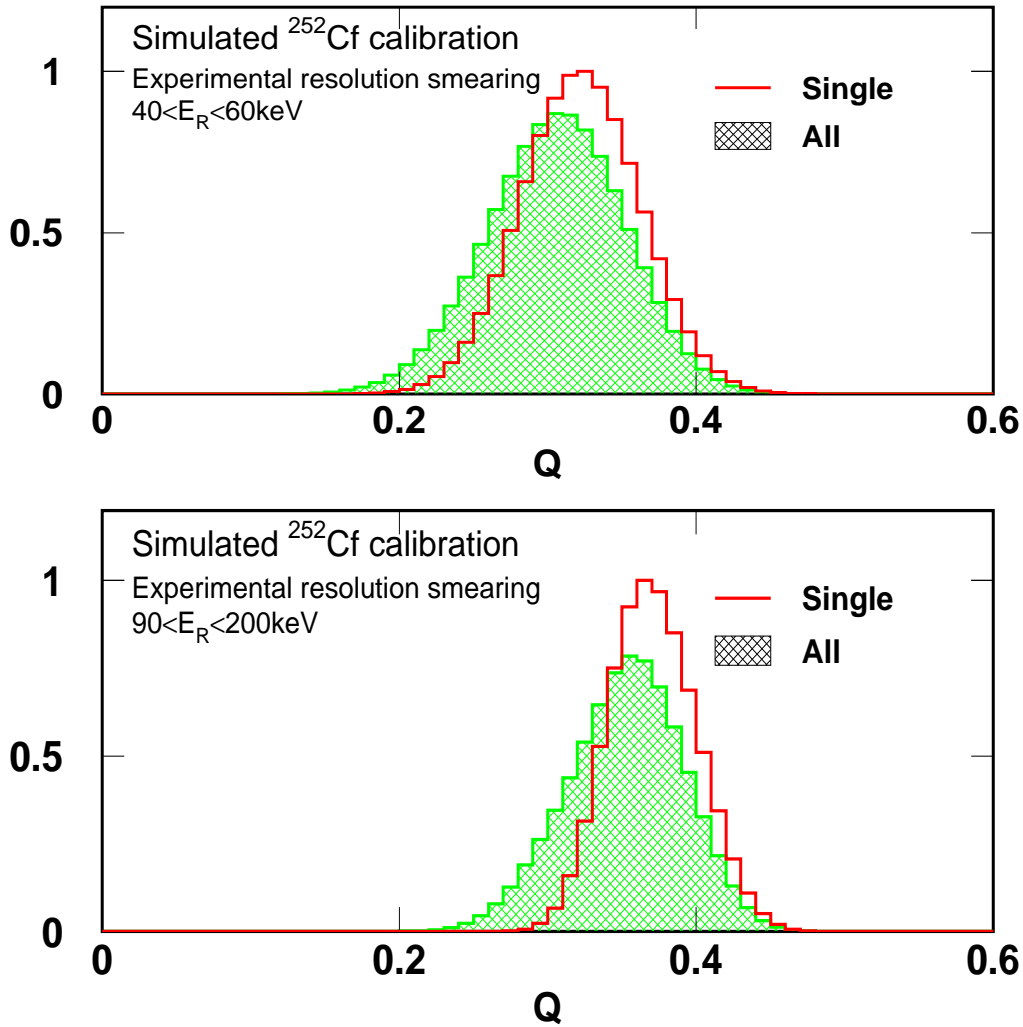


Figure 8: Normalized spectra of the Q variable for a GEANT simulation of a ^{252}Cf calibration, selecting (hatched area) or not (continuous line) single interactions, in the 40-60 keV (top panel) and 90-200 keV (bottom panel) energy ranges. The distribution corresponding to all interactions is slightly shifted down (~ 0.015 units between 20 and 200 keV) in regards to the single interactions distribution, and is only slightly broader.

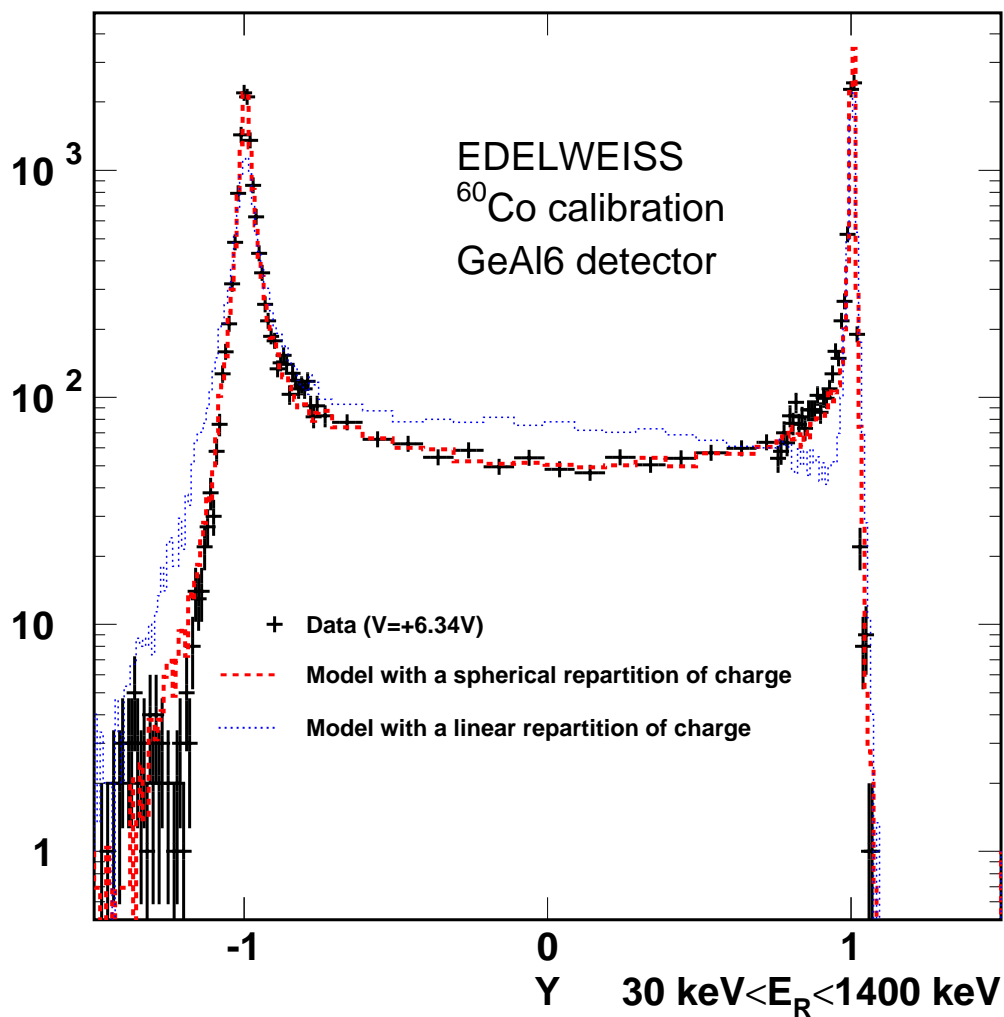


Figure 9: Distribution of the $Y = \frac{E_{guard} - E_{center}}{E_{guard} + E_{center}}$ variable for events of ⁶⁰Co calibration under +6,3 V bias voltage with $30 \text{ keV} < E_I < 1400 \text{ keV}$ (cross). The two other spectra correspond to the simulated distributions obtained for modelisations in the case of a charge reparted in a sphere (dashed, $r_b = 4.2 \text{ mm}$, $R_C = 24.5 \text{ mm}$) and charge reparted linearly (dotted, for parameters giving the same fiducial volume).

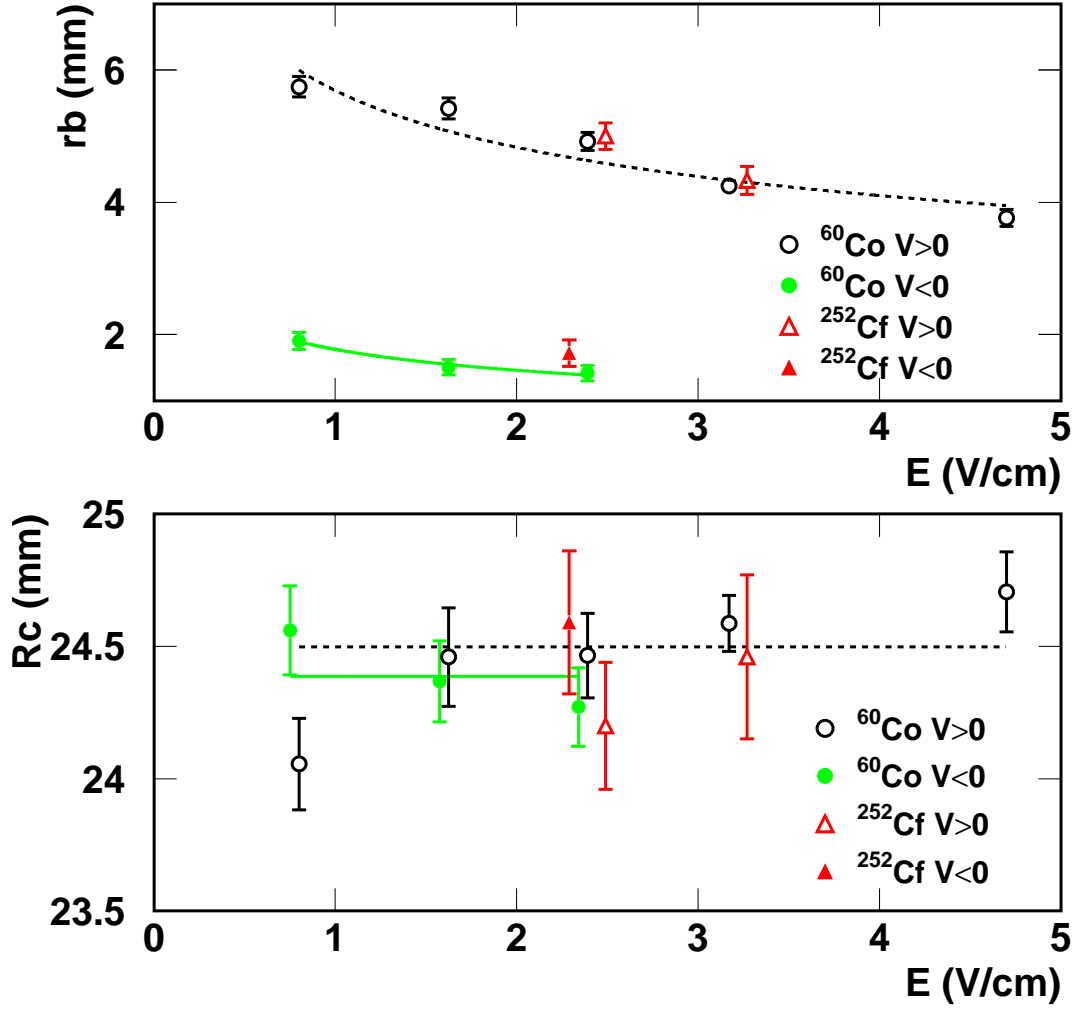


Figure 10: Optimized values for r_b (top pannel) and R_c (lower pannel) for ^{60}Co (circles) and ^{252}Cf (triangles) calibrations of the GeAl6 detector versus applied field values. Positive (negative) bias voltages correspond to the empty (filled) symbols. The r_b distribution is fitted by a power law: $r_b = aE^{-b}$. The fit gives $a_+ = 5.7 \pm 0.1$, $a_- = 1.8 \pm 0.1$, $b^+ = -0.24 \pm 0.02$ and $b^- = -0.28 \pm 0.09$.

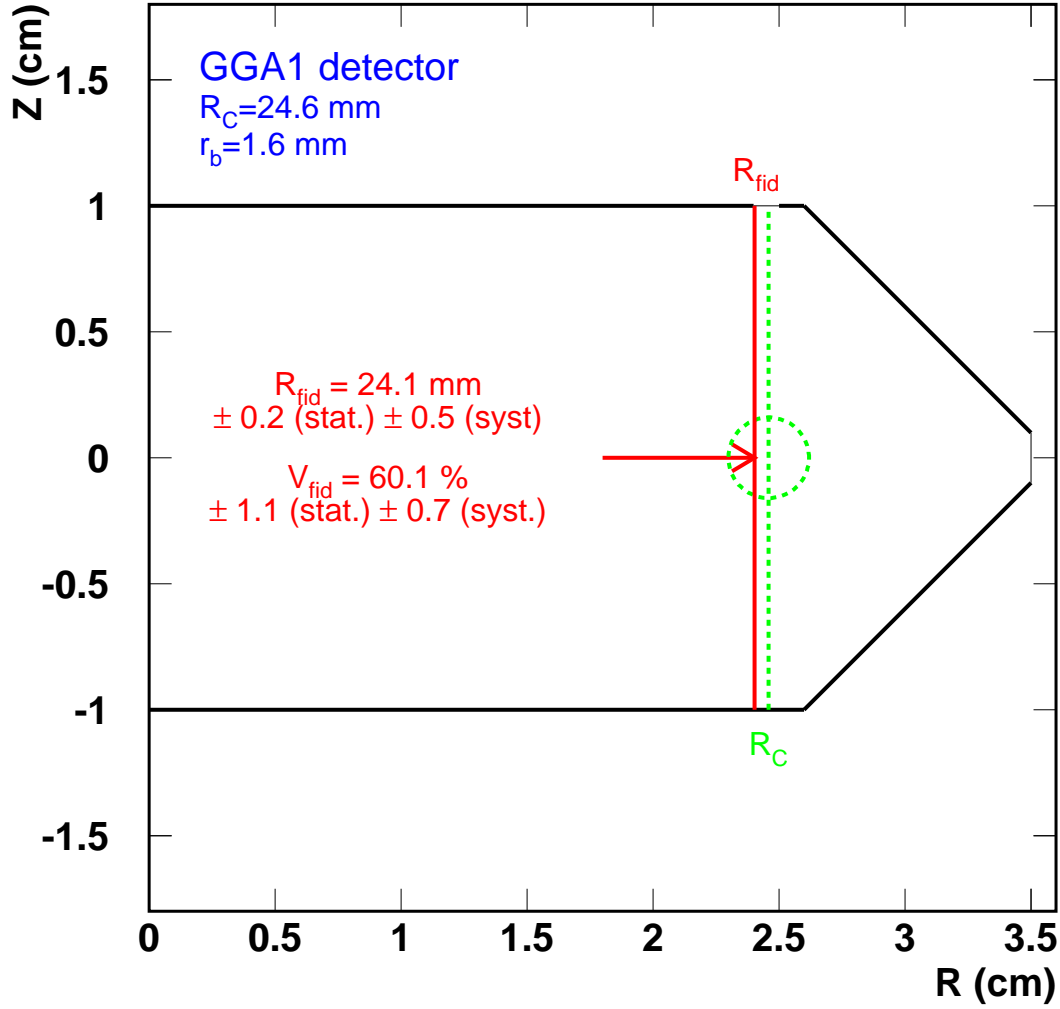


Figure 11: Representation of the GGA1 detector in the (R, Z) plane. The thick line corresponds to $R_{fid} = 24.1$ mm. Also shown is the line $R_C = 24.6$ mm delimiting the volumes associated with collection on the center and guard electrodes (dotted) and a circle of radius $r_b = 1.6$ mm centered on R_C (dotted). These values correspond to the optimum for a ^{252}Cf calibration of the GGA1 detector under a bias voltage of -4.00 V.